A modeling analysis of rainfall and water cycle by the cloud-resolving WRF model over western North Pacific

Wenhua Gao[1,2] and Chung-Hsiung Sui[2]

[1]National Satellite Meteorological Center, China Meteorological Administration, Beijing

[2]Department of Atmospheric Sciences, National Taiwan University, Taipei

Corresponding author address: Prof. Chung-Hsiung Sui, Department of Atmospheric Sciences, National Taiwan University, Taipei.

E-mail: sui@as.ntu.edu.tw

Abstract

This study simulates regional precipitation, especially extreme precipitation events, and the regional hydrologic budgets over the western North Pacific region during the period from May to June 2008 by the high-resolution (4-km grid spacing) Weather Research and Forecast (WRF v3.2.1) model with explicit cloud microphysics. The model initial and boundary conditions are derived from NCEP/DOE R2 reanalysis data.

Adopting the retrieved rainfall from Tropical Rainfall Measuring Mission (TRMM) 3B42 as a reference for comparison, the WRF simulations reproduce the spatial distributions of time mean precipitation amount and rainy days. But the simulated frequency distributions of rainy days and rainfall amount show overestimated light precipitation, underestimated moderate to heavy precipitation, and well simulated extreme precipitation. The vapor budget analysis shows that the heavy precipitation is contributed mostly by the stronger moisture convergence. However, in less convective periods, the precipitation is more influenced by the surface evaporation. The vapor budget is sensitive to the cloud microphysics scheme that affects the location and strength of atmospheric latent heating and then the large-scale circulation.

1. Introduction

Precipitation is an essential parameter describing the monsoon climate. The spatial distribution of precipitation indicates the location of atmospheric heat source, and the precipitation evolution reflects the variability of monsoon circulation system. Meanwhile, precipitation is also a key component of the earth's hydrological cycle. Studying precipitation characteristics is essentially important for understanding monsoon circulation and its relationship with other components of the hydrological cycle. However, an accurate simulation of summer precipitation, particularly for tropical regions, remains a major challenge due to the frequent local-scale convective activity [Jenkins, 1997; Kunkel et al., 2002]. Modeling and predicting the tropical atmosphere phenomena such as summer monsoons activity, tropical convection, and cloud microphysical variable are still deficient for the lack of fundamental knowledge over the tropic ocean.

The East Asian (EA) monsoon and western North Pacific (WNP) monsoon affect not only the regional climate but also the vicinity of the region and even the global climate through hydrological and energy exchange processes [Lau and Weng, 2002]. In the past two decades, many researches on the WNP summer monsoon by using the reanalysis data and satellite precipitation dataset had been conducted [Murakami and Matsumoto, 1994; Wang et al., 2001; Wang and LinHo, 2002; Conroy and Overpeck, 2011]. The climate over WNP region depends not only on the atmospheric, but also on the oceanic conditions of tropical and subtropical regions. So, the moisture transport and hydrological cycle over the EA-WNP region are more complex than those over other regions. For example, the sources of water vapor variations over the EA-WNP region commonly come from three areas: the northern Indian Ocean, the South China Sea (SCS, including the cross-equatorial transport), and the western North Pacific [Zhou and Yu, 2005; Ding and Sikka, 2006]. Furthermore, the spatial heterogeneity of rainfall in this region may respond nonlinearly to changes in forcing factors [Zhou et al., 2009]. For lack of conventional observations, to present, relatively few studies have been dedicated to the regional model performance over the WNP region. Our study will focus on the climatology during the onset of SCS-WNP summer monsoon in the period from May to June 2008.

It is known that the existing global general circulation models (GCMs) horizontal grid intervals are too coarse for applications at regional scale regimes [Leung et al., 2003; Giorgi, 2006]. To mitigate this problem, a dynamical downscaling strategy to obtain regional weather phenomena influenced by the local topography or small-scale atmospheric features has been conducted in many previous studies [Giorgi, 1990; Christensen et al., 1998; Liang et al., 2004; Kanamitsu and Kanamaru, 2007], in which GCM or reanalysis data are used to provide lateral boundary condition, sea surface temperature, and initial land-surface conditions for more spatially-detailed climatologically simulations over a region of interest. The dynamical downscaling method is supposed to retain the large-scale circulation, and is intended to add information on the smaller scales that the coarse-resolution global model could not generate [Castro et al., 2005]. Note that the regional models can add value, but for certain variables and locations. Winterfeldt et al. [2010] argued that the dynamical downscaling does not add value to the global reanalysis wind speed in open ocean areas because of the relatively homogeneous topography over the ocean. In addition, the effects of spatial resolution on regional climate simulations have been discussed extensively. Leung and Qian [2003] analyzed the results of 5 yr regional simulations for the Pacific Northwest and California, and demonstrated that the 13-km nest produces more realistic seasonal mean precipitation as well as more frequent heavy precipitation compared to the 40-km nest, which are in closer agreement with the observations. Kobayashi and Sugi [2004] showed that the climatology of synoptic scale phenomena is well represented and tropical cyclones occurred more frequently with higher intensities when increasing global model resolution, improving the simulation of Asian monsoon. Improving the precipitation simulation with higher spatial resolution was generally reported in many climate studies due to the detailed representation of terrain effects and spatial heterogeneity. But now, most of the regional climate simulations still use a relatively coarse grid resolution (about 10-40 km).

In addition, Randall et al. [2007] pointed out that the cumulus parameterization used in GCMs is another major cause of ambiguity for climate simulation. The details of cloud microphysics scheme are expected to be introduced into regional climate studies instead of the cumulus parameterization. A global cloud resolving simulation with a mesh size of a few kilometers was conducted using a nonhydrostatic icosahedral atmospheric model (NICAM) [Miura et al., 2007]. Satoh et al. [2008] showed that the relative occurrence of rainfall rate from NICAM is in agreement with that of the TRMM PR dataset for strong rains over the oceans. Tao et al. [2003] simulated the mesoscale convective systems over South China Sea with a regional climate model and a cloud-resolving model, and indicated that proper simulation of precipitation processes probably needs cloud-scale models. However, until recently, few models have been run with just explicit microphysics (without using cumulus parameterizations) and with fine enough grid spacing (1-4 km) to investigate the regional climate mechanisms.

The long-term goal of this study is to refine our understanding of clouds and precipitation over tropical Pacific warm pool and western North Pacific interacting with climate oscillations at seasonal or longer time scales. So the basic properties of simulated precipitation as well as regional water cycle in the high-resolution dynamical downscaling framework should be explored first. With this aim, several questions are addressed: (1) How well does the WRF high-resolution downscaling simulated precipitation agree with the observations over the WNP region? (2) Is the microphysics crucial for adequate performance of climatological precipitation over the ocean? (3) How well does the WRF model represent the regional hydrologic budgets?

The primary focus of this paper is to investigate the capability of cloud-resolving WRF model in simulating the characteristics of regional precipitation, especially extreme precipitation events as well as the regional hydrologic budgets over the western North Pacific. The paper is organized as following: Section 2 describes the model, data and experimental design. Section 3 examines the thermodynamic variables. The comparisons of observed and simulated daily mean precipitation, percentage of rainy days, precipitation frequency distribution and extreme precipitation are presented in section 4. The hydrologic budgets are discussed in section 5, and a summary is given in section 6.

2. Model, data and experimental design

2.1 Model description

The model employed here is the Weather Research and Forecast (WRF) model version 3.2.1 [Skamarock et al., 2008]. The WRF model is a mesoscale numerical weather system designed for short-term weather forecast as well as long-term climate simulation. It is a non-hydrostatic, terrain-following mesoscale model, and is being developed and studied by a broad community of researchers in the recent years.

The Chinese Academy of Meteorological Sciences (CAMS) two-moment microphysics is adopted in this study as an alternative microphysical scheme. It was developed by Hu and He [1988] and had been tested and employed in many previous studies [Hu and He, 1989; Lou et al., 2003; Li et al., 2008; Gao et al., 2011a, 2011b]. A total of 11 microphysical variables including the mixing ratio of vapor, the mixing ratios and number concentrations of cloud droplet, rain, cloud ice, snow, and graupel are predicted in CAMS microphysics. In the past years, the scheme has received many significant improvements, such as accurate calculation of supersaturation, detailed treatment of autoconversion and droplet nucleation parameterization. Gao et al. [2011b] evaluated and improved the CAMS raindrop microphysical parameterization against the Southwest Monsoon Experiment (SoWMEX) /Terrain-influenced

Monsoon Rainfall Experiment (TiMREX) observations in June 2008.

2.2. Validation dataset

The Tropical Rainfall Measuring Mission (TRMM) 3B42 rainfall estimation version 6, which is a high spatial (0.25° by 0.25°) and high temporal (3 h) satellite-derived precipitation dataset available in the latitude band 50^0S-50^0N from 1 January 1998 to present. These data are created by blending passive microwave data collected by low earth orbit satellites [such as TRMM Microwave Imager (TMI), Special Sensor Microwave Imager (SSM/I), Advanced Microwave Scanning Radiometer (AMSR), Advanced Microwave Sounding Unit (AMSU)], and the infrared (IR) data collected by the international constellation of geosynchronous earth orbit (GEO) based on calibration by the precipitation estimate of the TMI-PR combined algorithm. The physically based combined microwave estimates are used where available, and the remaining grid boxes are filled with microwave calibrated IR estimates [Huffman et al., 2007].

2.3 Experimental design

The model domain is designed to consist of three one-way nested domains as shown in Fig. 1. The numbers of grid points and corresponding horizontal grid resolutions for domains 1, 2, 3 are $290\times210\times35$ at 36-km, $541\times421\times35$ at 12-km and $883\times691\times35$ points at 4-km, respectively. The lateral boundary condition is specified at the lateral boundary grid points and the neighboring 4-grid relaxation zone. To capture the large-scale processes important for Pacific Northwest climate, the outermost domain encompasses nearly the entire East and Central Asia continent and much of the western Pacific Ocean. The use of such a large outer domain keeps the outer boundaries far from the innermost domain to ensure that weather systems approaching the Pacific Northwest are free from lateral boundary influences. The second nested domain covers the East Asia continent and the western North Pacific, capturing the tropical convections and East Asian monsoon circulations that influence the Pacific Northwest. The innermost domain covers the South China Sea and portions of the western North Pacific.

For non-hydrostatic cloud resolving models, the choice of horizontal and vertical grid resolutions is always an important issue. Different resolutions in such models can have a major impact on the resolved convective processes [Weisman et al. 1997; Tompkins and Emanuel 2000]. Weisman et al. [1997] suggested that a minimum grid length of 4 km is necessary to reasonably simulate the internal structures and mesoscale circulations of a midlatitude squall line. Tompkins and Emanuel [2000] suggested that a high vertical resolution (less than 33 hPa) is needed to develop a high degree of vertical structure in water vapor profiles and stratiform precipitation processes. The effect of resolution on simulated cloud systems has also been performed by evaluations of simulated clouds against observed cloud quantities [e.g. Johnson et al. 2002; Satoh et al. 2010, 2012 and references therein]. Satoh et al. [2010, 2012] compared the simulated cloud properties by a global cloud resolving model with a mesh sizes of 3.5, 7 and 14 km with satellite data. They found that the general characteristics of the cloud distribution are similar, but the cloud thickness and the size of the mesoscale convective system depend quantitatively on resolution. Based on the above considerations and on the limitation of the computer resources, we choose the mesh size of 4 km in the current study.

The initial and lateral boundary conditions are interpolated from the NCEP/DOE reanalysis 2 data (hereafter R2) [Kanamitsu et al., 2002]. The lateral boundary conditions are updated every 6 hours. The sea surface temperature (SST) from R2 data is also updated every 6 hours. The physics schemes used are Noah land surface model [Chen and Dudhia, 2001], Yonsei University (YSU) planetary boundary-layer scheme [Hong et al., 2006], Grell-Devenyi cumulus parameterization [Grell and Devenyi, 2002], rapid radiative transfer model long-wave radiation [Mlawer et al., 1997] and Dudhia short-wave radiation [Dudhia, 1989]. No cumulus parameterization is used in domain 3. In order to assess the impact of microphysics on the precipitation process in 4-km model resolution, two microphysics schemes are conducted: Goddard 3ICE [Tao and Simpson, 1993] and CAMS. Goddard 3ICE is a one-moment scheme, it predicts only the mixing ratios for five hydrometeor species. Goddard scheme is mainly based on Lin et al. [1983] with additional processes from Rutledge and Hobbs [1984]. Several modifications have been made in the past years. e.g., new saturation techniques [Tao et al., 2003] are added; all microphysical processes that do not involve melting, evaporation or sublimation are calculated based on one thermodynamic state; the sum of all sink processes associated with one species will not exceed its mass. Whereas, CAMS is a two-moment scheme, it predicts both the mixing ratios and number concentrations for five hydrometeor species (including droplet number).

The simulation period is from 0000 UTC 1 May to 2400 UTC 30 June 2008. The model is re-initialized every 2 days. Each re-initialization runs for 12 hours proceeding the initial time of each 2-day simulation by nudging the horizontal winds above 850 hPa at each grid toward the reanalysis values. The re-initialization is a simple spin-up run to produce a set of initial fields every two days in the two-month integration period to mitigate the climate drift in regional climate simulations [Dickinson et al., 1989; Qian et al., 2003]. Grid nudging is applied in the two outer model domains (D1 and D2) but not in the innermost domain (D3), which allows the mesoscale model to freely develop atmospheric structure at finer spatial scale. The model outputs at every 6 hours are used for the evaluation.

3. Evaluation of model thermodynamic variables

To evaluate the state variables, we compare the model simulated temperature and humidity with R2 data. Figure 2 shows the difference of mean dry static energy ($DSE = c_p T + gz$, where C_p is the specific heat at constant pressure, T absolute temperature, g the gravitational acceleration and z the height above surface) and latent heat energy ($L_v q$, where L_v is the latent heat of vaporization, q the water vapor mixing ratio) averaged over domain 3 during May to June 2008 between WRF simulations and R2 reanalysis. The value of DSE shown in Fig. 2 is determined mainly by the air temperature. The model simulated temperature by the two cloud schemes differ from the R2 data within $1^{o}C$, and the CAMS scheme simulated temperature is slightly warmer than that in Goddard scheme. Compared with the R2 data, the two simulations show a common warm bias in the upper troposphere above 200 hPa, and a common cold bias in the low troposphere below 850 hPa. Associated with the model cold bias in the lower troposphere, model results also show a common moist bias. But the two cloud schemes produce opposite moisture bias above 850 hPa. More latent heat release, which results in heating the atmosphere, is likely responsible for the warmer and more humid air above the boundary layer in CAMS scheme than those in Goddard scheme through the thermodynamic feedback processes. But the common moist and cold biases in the two WRF simulations are indicative of deficiencies in the model boundary layer process.

The diurnal cycles of model temperature and humidity are further examined by forming a diurnal composite of vertically integrated saturation water vapor mixing ratio (q_s) and water vapor mixing ratio (q) averaged over domain 3 from 30 consecutive two-day integrations during May to June 2008. The composite q_s and q are shown in Fig. 3a and 3b, respectively. Since q_s is function of temperature, the diurnal q_s from R2 shows a maximum value near 06 UTC (local time 3 pm) and a cooling trend toward a minimum value near 24 UTC (local time 9 am) with an amplitude of about 4 kg m^{-2}. The two WRF simulations show a similar diurnal change characterized by a warm phase near 06 to 12 UTC and a cold phase near 18 to 24 UTC with a smoother phase change and a weaker amplitude than that of R2 data. The difference between the simulated and assimilated q_s is clearly resulted from the cloud radiative interactions in the cloud-resolving physics. The higher q_s from CAMS scheme than that from Goddard scheme (by about 2 4 kg m^{-2}) is consistent with the difference in simulated DSE profiles shown in Fig. 2a. The composite curves of q for the model and R2 data show very weaker diurnal cycles with no consistent phase changes. This indicates that the water vapor field in the domain of interest is dominated by synoptic scale disturbances. The simulated q by CAMS is somewhat larger than that by Goddard, but the simulated precipitation by CAMS is significantly larger than that by Goddard which is correlated with the moisture convergence. This will be discussed in detail in section 5.

4. Evaluation of model precipitation

Precipitation is an important quantity for climate studies, and reducing the precipitation bias is one of the major goals for regional climate simulations. The TRMM 3B42 daily precipitation data are used as a reference in this study. The R2 reanalysis data and WRF simulations are spatially re-gridded onto 0.25 grid points, the same as the TRMM dataset, for comparison purpose. Note that no interpolation is used when calculating the precipitation frequency.

4.1 Mean precipitation pattern

Figure 4 shows the spatial distribution of time mean precipitation during May to June 2008 from TRMM observations, R2 reanalysis, and WRF simulations. The major monsoon rainbands are located over the Philippine Sea, South China Sea, and the southeast China coast. The location of rainfall center over the ocean is near the 9.5°N, 131°E, and the maximum value is about 21 mm day^{-1} (Figure 4a). The WRF simulations reproduce the characteristics of daily mean precipitation well with the TRMM observations. The patterns of spatial distribution from WRF model clearly show an improvement compared with R2 reanalysis, which has a wet bias over the ocean, and has a strong dry bias over the southeast China coast. The Goddard scheme reduces the wet bias of R2 reanalysis over the ocean; on the contrary, the CAMS scheme introduces a wet bias relative to R2 reanalysis. Although the CAMS scheme produces the maximum daily mean precipitation with a value about 21 mm day^{-1} over the ocean, similar to the TRMM observation, it overestimates the range of heavy precipitation. The spatial distributions of daily mean precipitation in Fig. 4 show that the two microphysics schemes produce similar precipitation patterns, but different precipitation amount.

To quantitatively evaluate the performances of WRF model in simulation of precipitation, the time mean precipitation averaged over domain 3, the pattern root mean square error (RMSE) and pattern correlation coefficients with respect to the TRMM observations are listed in Table 1. Also included in the Table is the time mean precipitation from the assimilation product R2. Results show that the simulated spatial and temporal mean precipitation in Goddard scheme is slightly less than observation, while that in CAMS scheme is somewhat larger than observation, indicating that climatological precipitation in the northwest Pacific warm monsoon season is sensitive to cloud microphysics scheme. This is consistent with the finding that the skill in simulating tropical precipitation systems is generally poorer than that in mid-latitude systems [Wang et al., 2003; Lee et al., 2004] due to weak baroclinic instability and complicated physical processes in East Asia. Table 1 further shows that the time mean patterns of precipitation simulated by the high-resolution WRF with the two microphysics schemes have smaller pattern RMSE and higher pattern correlation with the TRMM precipitation than that produced by R2. This indicates that the high resolution WRF with an explicit cloud microphysics can reasonably resolve mesoscale variability, and is capable of simulating accumulated precipitation distribution in properly designed regional climate downscaling simulation.

4.2 Temporal evolution of the precipitation

The model performances in reproducing the northward migration of tropical and subtropical fronts and associated rain bands are examined. Figure 5 shows the time-latitude cross-section of daily precipitation along the longitudinal band between 110° and 145°E. Two major phases of northward movement of convection zone from near the equator to about 25°N are observed (middle of May and end of June). The average speed of northward propagation is about 1.0° latitude per day. The northward movement reflects the seasonal migration of the EA-WNP monsoon rain bands. The WRF model and R2 reanalysis generally reproduce the two northward marches of rain bands. But, they all fail to simulate the weak northward rain band from 10° to 25°N in the period from end May to early June. In addition, the temporal correlation coefficients between TRMM observed and WRF simulated daily precipitation are similar to that between TRMM observed and R2 reanalysis (area averaged ～0.34), indicating that the current WRF downscaling simulation is not improving the temporary variability significantly. Since many atmospheric variability fields which lead to precipitation are constrained by observations twice a day in the reanalysis data, so no obvious improvements are made in the timing of precipitation.

4.3 Precipitation frequency

We next analyze frequency distributions of rainy days and precipitation. The percentages of all days with precipitation exceeding 0.1 mm day^{-1} (the definition of rainy day in this study) and 50 mm day^{-1} during May to June 2008 are calculated.

The percentage of rainy days is largely affected by the re-gridded data [Osborn and Hulme, 1997; Ensor and Robeson, 2008], which will potentially generate systematic biases in the comparison. For example, the averaged precipitation frequency of rainy days will increase about 15 % when using the re-gridded data instead of the original data in our study. So, we use the results from all the original model outputs and do not interpolate them to the resolution of TRMM observations when calculating the precipitation frequency. This approach helps to directly derive information from the model itself, especially for models with a relatively high resolution [Sun et al., 2006].

The percentage of rainy days in TRMM dataset is higher over the southernmost and northernmost of domain 3. The R2 reanalysis overestimates the frequency of rainy days over the ocean compared to the TRMM dataset. As we expect, the patterns of rainy day frequency are improved in WRF simulations than that in R2 reanalysis (Figure 6). The WRF simulations evidently reduce the percentage of rainy days in the southern part of domain and increase that in the northern part of domain, conforms to the TRMM observations. Note that the CAMS two-moment scheme produces a little more rainy days than that from Goddard one-moment scheme (there exist areas where the percentage of rainy days is less than 30%). This is attributed to the conclusion in Morrison et al. [2009] who found that two-moment microphysics can produce a wider spread of stratiform precipitation as a result of weaker rain evaporation rate below the melting layer compared to one-moment microphysics in the stratiform region. The rate of rain evaporation is associated with the difference in predicted rain size distribution intercept parameter (which is larger in the stratiform region than that in two-moment scheme but is specified as a constant in one-moment scheme). That is, the raindrop number concentration in two-moment scheme is usually less than that in one-moment scheme in the stratiform region, resulting in weaker rain evaporation rate. Additionally, the representation of cloud droplet concentration is probably another reason for the difference. Saleeby et al. [2010] showed an increase in aerosol concentration over the East China Sea by the discrepancies in rainfall estimates between the TRMM PR and TMI sensors. In CAMS scheme, similar increase of droplet concentration over domain 3 (reach up to 300 cm^{-3} sometimes) will reduce the autoconversion efficiency of cloud water to rain. As a result, raindrop number concentration decreases, mean raindrop diameter and collision coalescence rate increase, leading to high rainfall frequency during the rain formation process under the condition of sufficient water vapor. Li et al [2011] also revealed that the rainfall frequency increases with increasing condensation nuclei for high liquid water path (LWP).

Table 2 shows the mean precipitation amount, percentage of rainy days, and precipitation intensity (precipitation divided by percentage of rainy days) averaged over domain 3. Some previous studies have focus on these characters of precipitation [Dai, 2001; Sun et al., 2006]. The percentage of rainy days with precipitation exceeding 0.1 mm day^{-1} from TRMM dataset is 47.4%. The R2 reanalysis and WRF model outputs fall between 49.1 and 57.1%, which are a little larger than the TRMM observations. The percentage of rainy days from Goddard scheme tends to be lower than that from CAMS scheme as discussed above. As a result, the model precipitation intensities from R2 reanalysis and WRF simulations are slightly weaker than the TRMM precipitation intensity.

The percentage of days with heavy precipitation (exceeding 50 mm day^{-1}) is shown in Figure 7. Typical summer monsoon heavy rainbands are located over the Philippine Sea, South China Sea, and southeast China coast. The R2 reanalysis, limited by coarse resolution and cumulus parameterization, underestimates heavy rainfall events compared to the TRMM observations. The WRF downscaling simulations are evidently improved than that from R2 reanalysis, especially over southeastern China and South China Sea. However, CAMS scheme overestimates the frequency of heavy precipitation by up to 3-6 percentage points over the Philippine Sea, resulting in larger precipitation amount over there. Note that the broad feature of heavy precipitation frequency follows a similar spatial pattern compared to that of the daily mean precipitation (Figure 4), especially for the locations with maximum values. The maximum accumulated precipitation amount is clearly attributable to the heavy precipitation events.

To further examine the rainfall frequency distribution, the observed TRMM daily precipitation in the period of May to June 2008 within the domain 3 is partitioned into 12 bins (only the rainy days are included), covering the first nine decile bins (0-10%, 10-20%, ... 80-90%) and the 90-95%, 95-99%, and 99-100% bins. In the following discussions, 0-30% bin is taken as light precipitation; 30-60% bin as moderate precipitation; 60-90% bin as heavy precipitation; 90-100% bin as very heavy precipitation, and the top 1% as extreme precipitation.

In addition to the TRMM data, we also calculate the frequency distributions for model assimilated R2 and WRF simulated rainfall data. The daily precipitation at original grid resolution for the same period and domain from each datasets are used. The calculated frequency distributions are shown in Figure 8. For light precipitation especially the first percentile bin (precipitation rates between 0.1 and 0.6 mm day^{-1}), the WRF simulated frequency is much higher; while the assimilated frequency in R2 reanalysis is lower. For moderate to heavy precipitation, the WRF simulations are generally lower, and R2 reanalysis data show the opposite frequency. For the very heavy precipitation, R2 reanalysis data obviously underestimate, especially the top 1% extreme precipitation (great than 107.5 mm day^{-1}). The above features confirm the reasoning that the R2 reanalysis data cannot resolve the physical processes and mesoscale weather systems to produce extreme precipitation. The WRF simulated extreme events are in good agreement with the TRMM observations due to the cloud-resolving microphysics resolved in high resolution WRF model. Better representation of climate extreme is a key consideration for regional climate simulation, and the WRF results here show a reasonable skill and add more value to the downscaling approach in reproducing the very heavy precipitation.

The WRF simulated precipitation frequency by the two cloud schemes in Figure 8 show that the CAMS scheme produce less frequency in light rains and slightly more frequency in heavy rains compared with those from Goddard scheme. Note that only the days with precipitation amount exceeding 0.1 mm day^{-1} are included in the statistics. Li et al. [2011], using the observations at the Southern Great Plains (SGP) site during the summer seasons, suggested that light rains occur less frequently and heavy rains occur more frequently under polluted conditions than under clean conditions. The simulated cloud droplet concentrations in CAMS scheme can sometimes reach up to ～300×10^6 m^{-3} and are higher than the common value over the ocean (i.e., ～50×10^6 m^{-3}), to some extent like the real polluted conditions over NWP region [Berg et al. 2008]. In addition, the features of precipitation frequency distribution from R2 reanalysis are qualitatively opposite to those from WRF simulations, probably due to the cloud-resolving microphysics used in WRF model whereas the cumulus parameterization used in R2 reanalysis. The microphysics scheme usually produces larger area of stratiform precipitation than that from cumulus parameterization [Chin et al., 2010].

To investigate the distribution of precipitation amount, Figure 9 shows the observed and simulated percentage of precipitation amount in the two summer monsoon months over WNP region (Domain 3) as a function of precipitation rate. The bins used here represent the light (0-30%), moderate (30-60%), heavy (60-90%), and very heavy (90-95%, 95-99%, and 99-100%) precipitation, respectively. The TRMM observations exhibit a broad frequency distribution with the peak between 9.9 and 38.4 mm day^{-1} (the third bin, heavy rain). The WRF simulations produce slightly more light precipitation than the TRMM observations because of too much light rain days (Figure 8). The light precipitation contributes only about 3% of the total precipitation amount although the occurrence frequency is the highest. The total precipitation amount comes mainly from the heavy precipitation bin, and the R2 reanalysis overestimates the contribution of heavy precipitation to the total precipitation (～53%) because of higher occurrence frequency. In addition, the percentages for the very heavy precipitation (exceeding 56 mm day^{-1} above top 5%) in R2 reanalysis decrease rapidly, corresponding to the lower occurrence frequency of very heavy precipitation. On the contrary, the WRF simulated extreme amount (top 1%) is slightly stronger but close to the TRMM observations. The accumulated extreme precipitation amount is comparable to that of the moderate precipitation (the second bin).

One of the main advantages of dynamical downscaling identified in previous studies is about the improvement in simulating extreme events over land due to a more realistic representation of topography. Here our results show a notable improvement in simulated extreme precipitation over the ocean, apparently due to explicitly resolved cloud microphysics with high spatial resolution. Note that some heavy precipitation events over the southeast China coast are included in our analysis, but the majority of very heavy precipitating events occurred over the warm NW Pacific and the rainfall statistics shown in Fig. 8 and 9 is not expected to be affected.

5. Hydrologic budgets

In this section, the hydrologic budget is analyzed to further understand relevant precipitation processes. We calculate the atmospheric hydrologic budget averaged over domain 3 during May to June 2008 by the following conservations equation for water vapor [Peixoto and Oort, 1983]:

$$\frac{\partial}{\partial t}\frac{1}{g}\int_{p_s}^{0} q dp + \nabla \cdot \frac{1}{g}\int_{p_s}^{0} q\mathbf{V} dp = E - P \quad (1)$$

where q and **V** are specific humidity and horizontal wind vector at pressure level p, p_s is the surface pressure, the first two terms on the left hand side represent the tendency change of precipitable water and the moisture flux divergence, E and P on the right hand side are surface evaporation and precipitation. We use the 6 hourly reanalysis data and the model outputs to calculate the above budget terms.

Figure 10 shows the simulated daily mean moisture convergence, evaporation, precipitable water tendency, and precipitation by WRF with CAMS scheme. Results show that the spatial distribution of precipitation coincides with that of the moisture convergence, and evaporation has a near uniform distribution with a magnitude near half of the precipitation amount. This is similar to the result of Xue et al. [2004] who investigated the monsoon development over East Asia and West Africa, and found that the monsoon precipitation is related more closely to the moisture convergence field rather than surface evaporation.

Integration of Eq. (1) over the region specified as the domain 3 in the WRF experiments yields:

$$MC = P - E + dW \quad (2)$$

Eq. (2) states the total amount of water vapor that enters the domain (MC) should be balanced with the precipitation (P) and precipitable water tendency (dW) minus evaporation (E) [Wang and Yang, 2008]. Figure 11 exhibits the time evolutions of the four moisture budget terms in Eq. (2) from R2 reanalysis and WRF simulations. The red line denotes the residual term (MC_{res}) defined as the sum of the three terms on the right-hand side of Eq. (2). Results show that the water vapor convergence in R2 forcing fields somewhat differs from the residual term MC_{res} (Figure 11a). This imbalanced water vapor budget in the reanalysis data is mainly induced by the artificial nudging process [Roads et al., 2002]. The imbalance here is small because the budget is averaged mostly over the ocean relative to budget over the land surface that can be made up of mountain, various vegetation etc., and cause large difference in surface heating. The calculated budgets using the two WRF outputs are balanced with vapor convergence (MC) in close agreement with MC_{res} (Fig. 11b and 11c). The temporal mean vapor budget terms in Eq. (2) for the period of May to June 2008 (Table 3) show that values of evaporation in R2 reanalysis and WRF simulations are similar (near 4 mm day^{-1}); however, the moisture convergence in CAMS scheme is about 3 times stronger than that in Goddard scheme. Consequently, the simulated total precipitation in CAMS scheme is larger than that in Goddard microphysics scheme. This is more evident in Fig. 11 during the periods of heavy precipitation in the middle of May and end of June, the precipitation intensity is quite consistent with the amount of moisture convergence, corresponding to the strong monsoon rainbands and tropical cyclone activities reported in Figure 5, indicating that the heavy precipitation events are contributed mainly by the stronger moisture convergence. During less convective periods, the mean evaporation contributes more to the mean precipitation amount than the moisture convergence. The magnitude of mean precipitation with Goddard scheme during these periods is almost the same as that of evaporation.

Figure 12 shows the mean moisture flux vector (m kg s^{-1} kg^{-1}) at 850 hPa and the corresponding moisture flux convergence fields (mm day^{-1}) averaged over May and June 2008 derived from R2 reanalysis, and WRF simulations. The patterns of moisture flux convergence are generally in agreement with that of daily mean precipitation (Figure 4), implying that the spatial distribution of precipitation is mainly decided by the moisture convergence field. Two major flows of water vapor transport are evident in the region of analysis. One comes from the Bay of Bengal, entering into southeastern China and the subtropical WNP region through the South China Sea; the other comes from the tropical western Pacific, entering the subtropics along the western edge of the WNP subtropical high. The wind direction near the southern boundary in Goddard scheme (Fig. 12b) is almost easterly, resulting in less water vapor transport into the domain compared to that from CAMS scheme. In addition, the WRF simulations show weaker moisture convergence over the western South China Sea and stronger moisture convergence over the southeastern China compared with that in R2 reanalysis. But, the WRF simulations are quite different over the WNP region. The moisture convergence from CAMS scheme is stronger than that from Goddard scheme because of the differences in simulated wind fields.

Although the two WRF simulations are subject to the same boundary forcing from the R2 reanalysis, the two microphysics schemes cause considerable differences in the simulated location and strength of precipitation and atmospheric latent heating, which in turn significantly modify the large-scale circulation. As a result, the CAMS scheme produces stronger moisture convergence than the R2 reanalysis, and the Goddard scheme produces weaker moisture convergence. The downscaling results suggest the importance of convective heating in summer monsoon climate over the WNP region. This is consistent with tropical wave dynamics that latent heat release is a dominant forcing that drives the large-scale circulation [Chang et al., 1982]. So, a proper representation of model microphysics is critical in simulating rainfall distribution and latent heating which is as important as the large-scale dynamics governing tropical waves, monsoon surges, and climate oscillations in the tropical and NW Pacific climate region.

6. Summary and conclusion

Precipitation is a key climate quantity, and reducing the precipitation bias is one of the major goals for improving climate simulations. In this paper, we evaluate the capability of the cloud-resolving WRF via a dynamical downscaling approach, on simulating regional precipitation, especially extreme precipitation events and the regional hydrologic budgets over the western North Pacific. The period of study is from May to June 2008, the period of transition from the onset of South China Sea monsoon to the WNP summer monsoon.

Our analysis indicates that the R2 reanalysis data well represents the large-scale characteristics of daily mean precipitation over the WNP region, but not the spatial distribution of precipitation revealed in the TRMM observations dominated by extreme rainfall events. This is due to the low resolution and parameterized convective processes in R2 reanalysis which inadequately resolve mesoscale precipitating features and smooth out the extreme events. The WRF downscaling simulations, however, reasonably produce more detailed spatial distribution of daily mean precipitation as reflected by higher pattern correlation coefficients and smaller pattern RMSE with the TRMM observations.

The percentage of rainy day (exceeding 0.1 mm day^{-1}) from WRF simulations are evidently improved than that from R2 reanalysis data. The CAMS scheme produces a little more rainy days than that from Goddard scheme. This is attributed to the two-moment microphysics in CAMS causing widespread stratiform precipitation due to weaker evaporation of rainwater below the melting layer relative to the one-moment microphysics in Goddard. Meanwhile, the spatial patterns of rainy days with precipitation exceeding 50 mm day^{-1} from WRF simulations are similar to the spatial patterns of daily mean precipitation, indicating that the maximum accumulated precipitation amount is mainly contributed by heavy precipitation events. In addition, the WRF simulations overestimate the frequency of light precipitation, somewhat underestimate the frequency of moderate to heavy precipitation, but well represent the frequency of very heavy precipitation, compared with the frequency distribution from TRMM data.

The moisture convergence from WRF simulations balances with the sum of precipitation and precipitable water tendency minus evaporation. During more convective periods, the precipitation amount is primarily contributed by moisture convergence. In less convective periods, the precipitation amount is more contributed by evaporation. The WRF simulations with these two microphysics schemes produce significantly different budget balance. Compared with the R2 budget, the moisture convergence is smaller in the Goddard scheme but larger in the CAMS scheme. The significant difference in simulated vapor budgets indicates the importance of resolving convection in tropical monsoon region that affects the precipitation, atmospheric latent heating and then the large-scale circulation.

Acknowledgments. The authors are grateful to all colleagues and students who contributed to this study. We acknowledge the computer resources provided by Prof. Sui's cluster in National Taiwan University and high performance computer center in National Central University. The authors also thank the anonymous reviewers for their constructive comments that improved this paper significantly. C.-H. Sui was supported by the National Science Council 100-2745-M-002-003-ASP. W.H. Gao was supported by xxxxxx.

References

Berg, W., T. L’Ecuyer, and S. van den Heever (2008), Evidence for the impact of aerosols on the onset and microphysical properties of rainfall from a combination of satellite observations and cloud resolving model simulations, *J. Geophys. Res.*, 113, D14S23, doi:10.1029/2007JD009649.

Castro, CL, RA Sr Pielke, and G Leoncini (2005), Dynamical downscaling: assessment of value retained and added using the regional atmospheric modeling system (RAMS), *J. Geophys. Res.*, 110, D05108, doi:10.1029/2004JD004721.

Chang, C. B., D. J. Perkey, and C. W. Kreitzberg (1982), A numerical case study of the effects of latent heating on a developing wave cyclone, *J. Atoms. Sci.*, 39, 1555-1570.

Chen, F., and J. Dudhia (2001), Coupling an advanced land-surface/ hydrology model with the Penn State/ NCAR MM5 modeling system. Part I: Model description and implementation, *Mon. Wea. Rev.*, 129, 569-585.

Chin, Hung-Neng S., P. M. Caldwell, and D. C. Bader (2010), Preliminary study of california wintertime model wet bias, *Mon. Wea. Rev.*, 138, 3556-3571.

Christensen, OB, J.H. Christensen, B. Machenhauer, and M. Botzet (1998), Very high-resolution regional climate simulations over Scandinavia-Present climate, *J. Climate*, 11, 3204-3229.

Conroy, J. L. and J. T. Overpeck (2011), Regionalization of present-day precipitation in the greater monsoon region of Asia*, *J. Climate*, 24, 4073-4095.

Dai, A. (2001), Global precipitation and thunderstorm frequencies. Part I: Seasonal and interannual variations, *J. Climate*, 14, 1092-1111.

Dickinson, R. E., R. M. Errico, F. Giorgi, and G. T. Bates (1989), A regional climate model for the western United States, *Climate Change*, 15, 383-422.

Ding, Y.H., and DR Sikka (2006), Synoptic systems and weather, *The Asian monsoon*, B. Wang, Ed., Praxis Publishing Ltd., Chichester, 131-202.

Dudhia, J. (1989), Numerical study of convection observed during the winter monsoon experiment using a mesoscale two-dimensional model, *J. Atmos. Sci.*, 46, 3077-3107.

Ensor, A. Leslie, and S. M. Robeson (2008), Statistical characteristics of daily precipitation: comparisons of gridded and point datasets, *J. Appl. Meteor. Climatol.*, 47, 2468-2476.

Gao, W.H., F. S. Zhao, Z. J. Hu, and X. Feng (2011a), A two-moment bulk microphysics scheme coupled with a mesoscale model WRF: Model description and first results, *Adv. Atmos. Sci.*, 28, 1184-1200.

Gao, W.H., C-H Sui, T-C Chen Wang, W-Y Chang (2011b), An evaluation and improvement of microphysical parameterization from a two-moment cloud microphysics scheme and SoWMEX/TiMREX observations, *J. Geophys. Res.*, 116, D19101, Doi:10.1029/2011JD015718.

Giorgi, F. (1990), Simulation of regional climate using a limited area model nested in a general circulation model, *J Climate,* 3, 941-963.

Giorgi, F. (2006), Regional climate modeling: Status and perspectives, *J. Phys. IV France*, 139, 101-118.

Grell, G. A., and D. Devenyi (2002), A generalized approach to parameterizing convection combining ensemble and data assimilation techniques, *Geophys. Res. Lett.*, 29(14), 1693, doi:10.1029/2002GL015311.

Hong, S.-Y., and Y. Noh, and J. Dudhia (2006), A new vertical diffusion package with an explicit treatment of entrainment processes, *Mon. Wea. Rev.*, 134, 2318-2341.

Hu, Z.J., and G. He (1988), Numerical simulation of microphysical processes in cumulonimbus, part 1: Microphysical model, *Acta Meteorol. Sin.*, 2(4), 471-489.

Hu, Z.J., and G. He (1989), Numerical simulation of microphysical processes in cumulonimbus, part 2: Case studies of shower, hailstorm and torrential rain, *Acta Meteorol. Sin.*, 3(2), 185-199.

Huffman, G. J., R. F. Adler, D. T. Bolvin, G. Gu, E. J. Nelkin, K. P. Bowman, E. F. Stocker, and D. B. Wolff (2007), The TRMM multisatellite precipitation analysis (TMPA): Quasi-global, multiyear, combined-sensor precipitation estimates at fine scale, *J. Hydrometeor.*, 8, 38-55.

Jenkins, GS (1997), The 1988 and 1990 summer season simulations for West Africa using a regional climate model, *J. Climate*, 10, 1255-1272.

Johnson, D., W.-K. Tao, J. Simpson, and C.-H. Sui (2002), A study of the response of deep tropical clouds to mesocale processes, Part I: Modeling strategy and simulation of TOGA COARE convective systems, *J. Atmos. Sci.*, 59, 3492-3518.

Kanamitsu, M., W. Ebisuzaki, J. Woollen, S-K Yang, J.J. Hnilo, M. Fiorino, and G.L. Potter (2002), NCEP-DOE AMIP-II Reanalysis (R-2), *Bull. Amer. Meteor. Soc.*, 83, 1631-1643.

Kanamitsu, M., and H. Kanamaru (2007), Fifty-seven-year California reanalysis downscaling at 10 km (CaRD10). Part I: system detail and validation with observations, *J. Climate*, 20, 5553-5571.

Kobayashi, C., and M. Sugi (2004), Impact of horizontal resolution on the simulation of the Asian summer monsoon and tropical cyclones in the JMA global model, *Climate Dyn.*, 93, 165-176.

Kunkel, KE, K Andsager, XZ Liang, RW Arritt, ES Takle, WJ Jr Gutowski, Z. Pan (2002), Observations and regional climate model simulations of heavy precipitation events and seasonal anomalies: a comparison, *J Hydrometeor.* 3, 322-334.

Lau, KM, HY. Weng (2002), Recurrent teleconnection patterns linking summertime precipitation variability over East Asia and North America, *J. Meteor. Soc. Japan*, 80, 1309-1324.

Lee, D.-K., D.-H. Cha, and H.-S. Kang (2004), Regional climate simulation of the 1998 summer flood over East Asia, *J. Meteor. Soc. Japan*, 82, 1735-1753.

Leung, L. R., L. O. Mearns, F. Giorgi, and R. L. Wilby (2003), Regional climate research, *Bull. Amer. Meteorol. Soc.*, 84, 89-95.

Leung, L. R., and Y. Qian (2003), The sensitivity of precipitation and snowpack simulations to model resolution via nesting in regions of complex terrain, *J. Hydrometeor.*, 4, 1025-1043.

Li, G., Y. Wang, and R. Zhang (2008), Implementation of a two-moment bulk microphysics scheme to the WRF model to investigate aerosol-cloud interaction, *J. Geophys. Res.*, 113, D15211, doi:10.1029/2007JD009361.

Li, Z., F. Niu, J. Fan, Y. Liu, D. Rosenfeld, and Y. Ding (2011), Long-term impacts of aerosols on the vertical development of clouds and precipitation, *Nature Geoscience*, 4, 888-894.

Liang XZ, L Li, KE Kunkel, M Ting, JXL Wang (2004), Regional climate model simulation of U.S. precipitation during 1982-2002. Part I: annual cycle, *J. Climate*, 17, 3510-3529.

Lin, Y.-L., R. D. Farley, and H. D. Orville (1983), Bulk parameterization of the snow field in a cloud model, *J. Climate Appl. Meteor.*, 22, 1065-1092.

Lou, X., Z. Hu, Y. Shi, P. Wang, and X. Zhou (2003), Numerical simulations of a heavy rainfall case in south China, *Adv. Atmos. Sci.*, 20(1), 128-138.

Miura, H., M. Satoh, T. Nasuno, A. T. Noda, and K. Oouchi (2007), A Madden-Julian oscillation event simulated by a global cloud-resolving model, *Science*, 318, 1763-1765, doi:10.1126/science.1148443.

Mlawer, E. J., S. J. Taubman, P. D. Brown, M. J. Iacono, and S. A. Clough (1997), Radiative transfer for inhomogeneous atmosphere: RRTM, a validated correlated-k model for the longwave, *J. Geophys. Res.*, 102, D14, 16663-16682.

Morrison, H., G.. Thompson, and V. Tatarskii (2009), Impact of cloud microphysics on the development of trailing stratiform precipitation in a simulated squall line: Comparison of one- and two-moment schemes, *Mon. Wea. Rev.*, 137, 991-1007.

Murakami, T., and J. Matsumoto (1994), Summer monsoon over the Asian continent and western north Pacific, *J. Meteor. Soc. Japan*, 72, 719-745.

Osborn, TJ, and M. Hulme (1997), Development of a relationship between station and grid-box rainday frequencies for climate model evaluation, *J. Climate*, 10, 1885-1908.

Peixoto, J. P., and A. H. Oort (1983), The atmospheric branch of the hydrological cycle and climate, *Variations in the Global Water Budget*, A. Street-Perrott, M. Beran, and R. Ratcliff, Ed., Reidel, 5-65.

Qian, J.-H., A. Seth, and S. Zebiak (2003), Reinitialized versus continuous simulations for regional climate downscaling, *Mon. Wea. Rev.*, 131, 2857-2874.

Randall, D. A., and Coauthors (2007), Climate models and their evaluation, *Climate Change 2007: The physical science basis*, S. Solomon et al. Ed., Cambridge Univ. Press, New York, 589-662.

Roads, J., M. Kanamitsu, R. Stewart (2002), CSE water and energy budgets in the NCEP-DOE reanalysis II, *J. Hydrometeor*, 3, 227-248.

Rutledge, S. A., and P. V. Hobbs (1984), The mesoscale and microscale structure and organization of clouds and precipitation in midlatitude cyclones. XII: A diagnostic modeling study of precipitation development in narrow cloud-frontal rainbands, *J. Atmos. Sci.*, 20, 2949-2972.

Saleeby, S. M., W. Berg, S. van den Heever, and T. L'Ecuyer (2010), Impact of cloud-nucleating aerosols in cloud-resolving model simulations of warm-rain precipitation in the East China Sea, *J. Atmos. Sci.*, 67, 3916-3930.

Satoh, M., T. Nasuno, H. Miura, H. Tomita, S. Iga, and Y. Takayabu (2008), Precipitation statistics comparison between global cloud resolving simulation with NICAM and TRMM PR data, *High Resolution Numerical Modelling of the*

Atmosphere and Ocean, W. Ohfuchi and K. Hamilton Ed., Springer, New York, 99-112.

Satoh, M., T. Inoue, and H. Miura (2010), Evaluations of cloud properties of global and local cloud system resolving models using CALIPSO and CloudSat simulators, *J. Geophys. Res.*, 115, D00H14, doi:10.1029/2009JD012247.

Satoh, M., S.-I. Iga, H. Tomita, Y. Tsushima, and A. T. Noda (2012), Response of upper clouds in global warming experiments obtained using a global nonhydrostatic model with explicit cloud processes, *J. Climate*, 25, 2178-2191.

Skamarock, W. C., J. B. Klemp, J. Dudhia, D. O. Gill, D. M. Barker, W. Wang, and J. G. Powers (2008), A description of the advanced research WRF version 3. NCAR Technical Note, NCAR/TN-475+STR, 123pp. Available at: http://www.mmm.ucar.edu/wrf/users/docs/arw_v3.pdf.

Sun, Y., S. Solomon, A. Dai, and R. Portmann (2006), How often does it rain? *J. Climate*, 19, 916-934.

Tao, W.-K., and J. Simpson (1993), The Goddard cumulus ensemble model. Part I: Model description, *Terr. Atmos. Oceanic Sci.*, 4, 35-72.

Tao, W.-K., J. Simpson, D. Baker, S. Braun, M.-D. Chou, B. Ferrier, D. Johnson, A. Khain, S. Lang, B. Lynn, C.-L. Shie, D. Starr, C.-H. Sui, Y. Wang, and P. Wetzel (2003) Microphysics, radiation and surface processes in the Goddard Cumulus Ensemble (GCE) model, *Meteor. and Atmos. Phys.*, 82, 97-137.

Tao, W.-K., Y. Wang, J.-H. Qian, C.-L. Shie, K.-M. Lau, and R.Kakar (2003), Mesoscale convective systems during SCSMEX: Simulations with a regional climate model and a cloud-resolving model. Weather and Climate Modeling: *INDO-U.S. Climate Research Program*, V. Singh, S. Basu, and T. N. Krishnamurti, Ed., New Age International, p18.

Tompkins, A. M., and K. A. Emanuel (2000) The vertical resolution sensitivity of simulated equilibrium temperature and water-vapour profiles, *Quart. J. Roy. Meteor. Soc.*, 126, 1219-1238.

Waliser, D. E., and M. Moncrieff (2008), The Year of Tropical Convection (YOTC) Science Plan: A joint WCRP-WWRP/THORPEX International Initiative. WMO/TD No.1452, WCRP-130, WWRP/THORPEX-No.9, WMO, Geneva, Available at: http://www.ucar.edu/yotc/documents/YOTC_Science_Plan.pdf.

Wang, B., R. Wu, and K.-M. Lau (2001), Interannual variability of the Asian summer monsoon: Contrasts between the Indian and the western North Pacific-East Asian monsoons, *J. Climate*, 14, 4073-4090.

Wang, B., and LinHo (2002), Rainy season of the Asian-Pacific summer monsoon, *J. Climate*, 15, 386-398.

Wang, B., and H. Yang (2008), Hydrological issues in lateral boundary conditions for regional climate modeling: Simulation of East Asian summer monsoon in 1998, *Climate Dyn.*, 31, 477-490.

Wang, Y., O. L. Sen, and B. Wang (2003), A highly resolved regional climate model (IPRC-RegCM) and its simulation of the 1998 severe precipitation event over China: I. Model description and verification of simulation, *J. Climate*, 16, 1721-1783.

Weisman, M. L., W. C. Skamarock and J. B. Klemp (1997), The resolution dependence of explicitly modeled convective systems, *Mon. Wea. Rev.*, 125, 527-548.

Winterfeldt, J., B. Geyer and R. Weisse (2010), Using QuikSCAT in the added value assessment of dynamically downscaled wind speed, *Int. J. Climatol.*, 31, 1028-1039, doi:10.1002/joc.2105.

Xue, Y., H.-M. H. Juang, W.-P. Li, S. Prince, R. DeFries, Y. Jiao, and R. Vasic (2004), Role of land surface processes in monsoon development: East Asia and West Africa, *J. Geophys. Res.*, 109, D03105, doi:10.1029/2003JD003556.

Zhou, T.J., and R.C. Yu (2005), Atmospheric water vapor transport associated with typical anomalous summer rainfall patterns in China, *J Geophys Res*, 110, D08104, doi:10.1029/2004JD005413.

Zhou, T.J., and Coauthors (2009), The CLIVAR C20C project: Which components of the Asian–Australian monsoon circulation variations are forced and reproducible? *Climate Dyn.*, 33, 1051-1068.

List of Figures:

Figure 11. Time evolution of the daily mean moisture budget averaged over domain 3 from (a) R2 reanalysis, (b) Goddard, and (c) CAMS simulations.

Figure 12. Mean 850 hPa moisture flux vector (m kg s^{-1} kg^{-1}) with associated moisture convergence fields (mm day^{-1}) averaged over May and June 2008 from (a) R2 reanalysis, (b) Goddard, and (c) CAMS simulations.

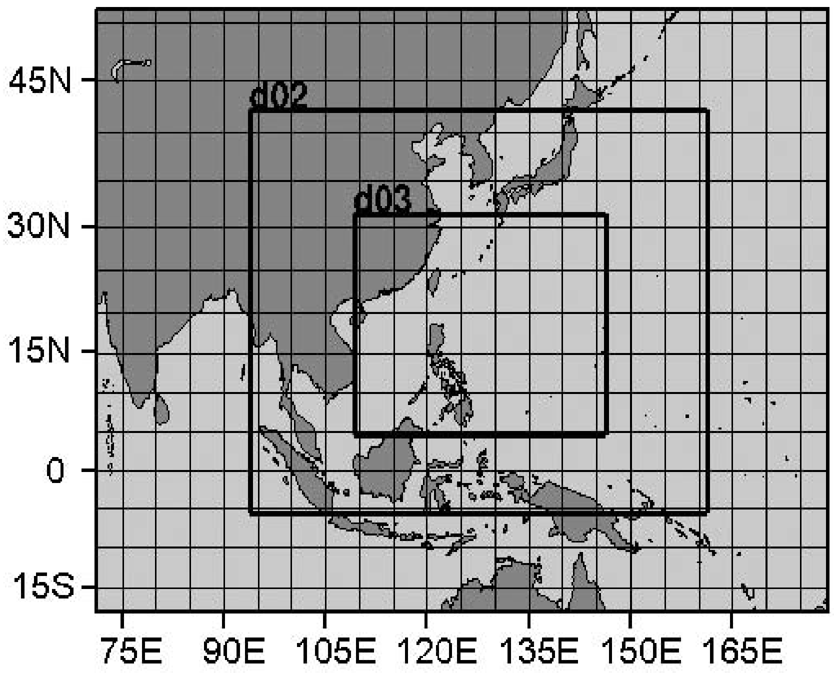

Figure 1. Geographic locations of the three domains used in the numerical simulation.

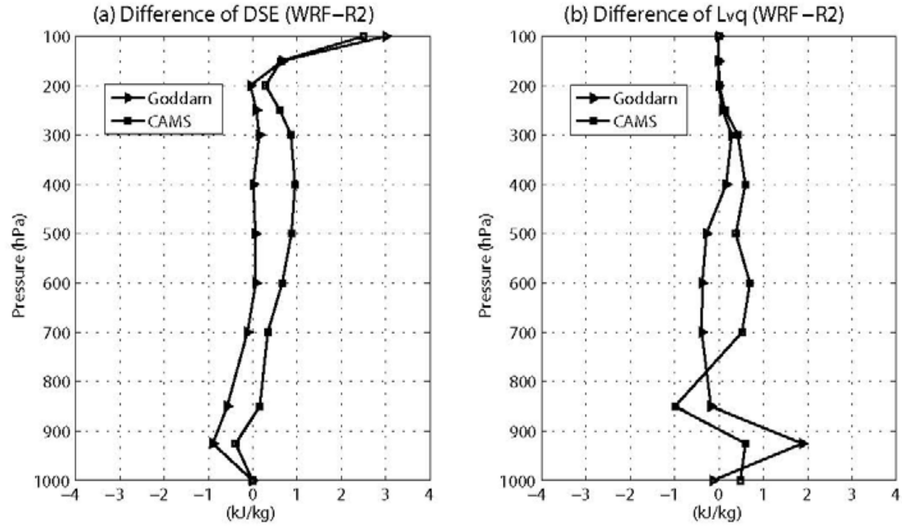

Figure 2. The difference of (a) DSE and (b) $L_v q$ (kJ kg^{-1}) between the WRF simulations and R2 reanalysis

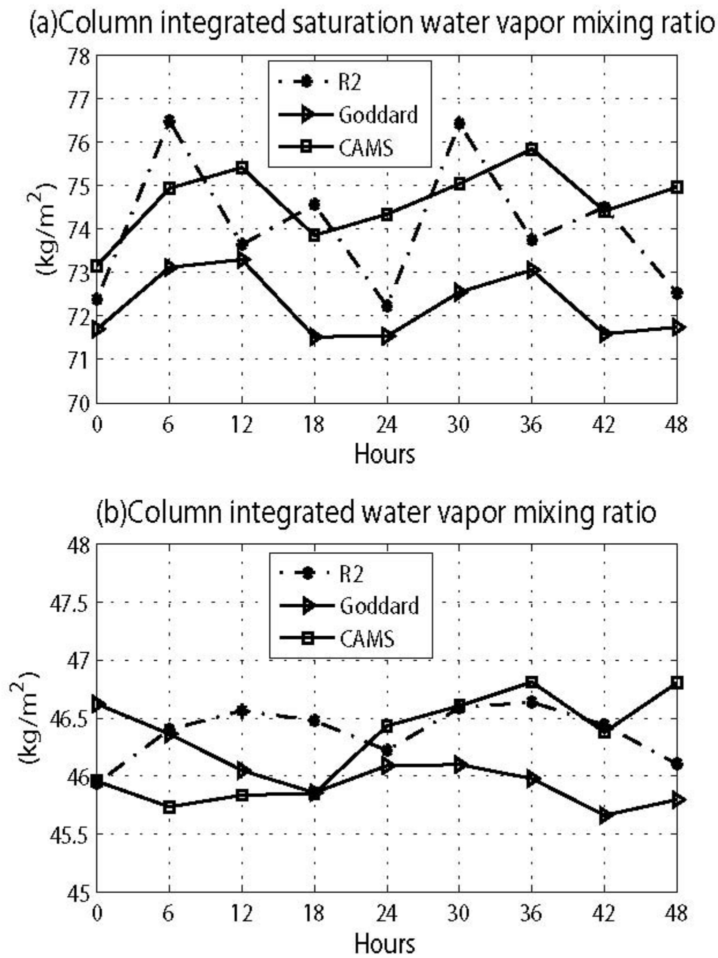

Figure 3. The diurnal composites of vertically integrated (a) saturation water vapor mixing ratio and (b) water vapor mixing ratio averaged over domain 3 from 30 consecutive two-day integrations

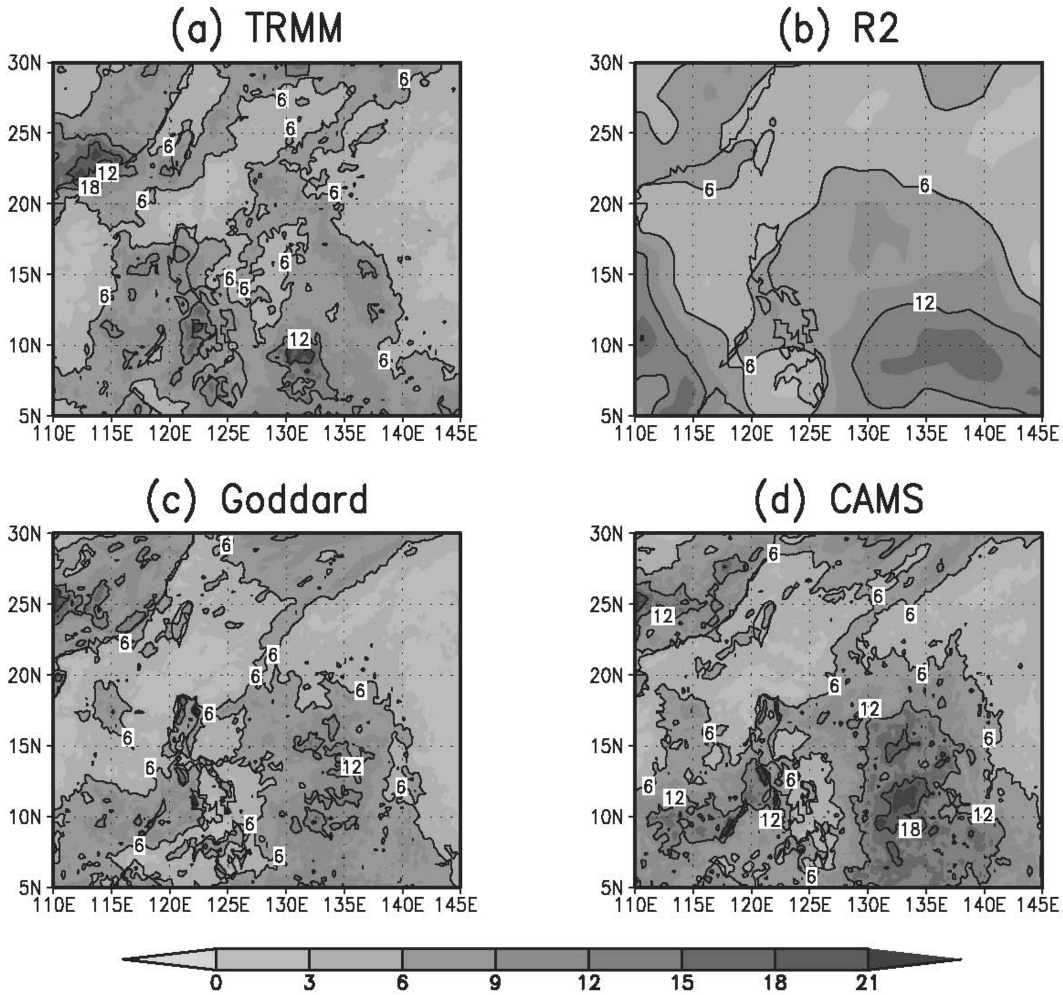

Figure 4. Spatial distribution of the daily mean precipitation (mm day^{-1}) during May to June 2008 from (a) TRMM, (b) R2 reanalysis, and (c), (d) WRF simulations.

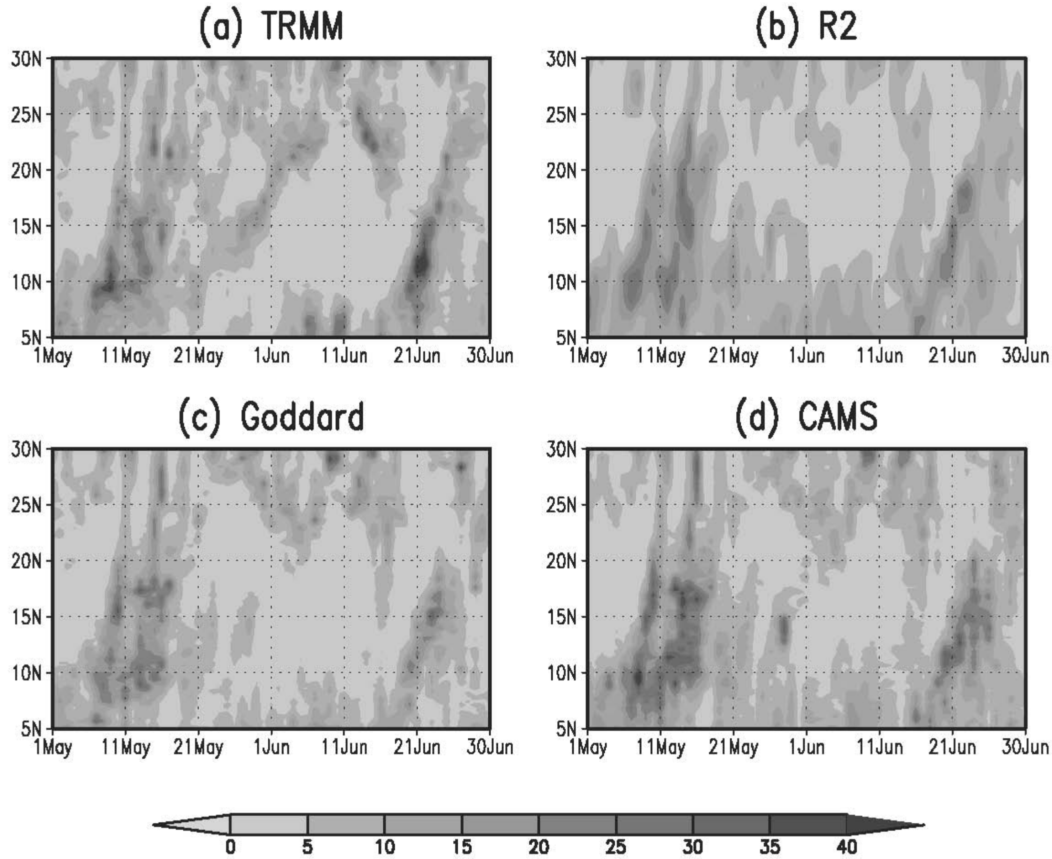

Figure 5. Precipitation (mm day^{-1}) as a function of time and latitude averaged over 110°-145°E from (a) TRMM, (b) R2 reanalysis, and (c), (d) WRF simulations.

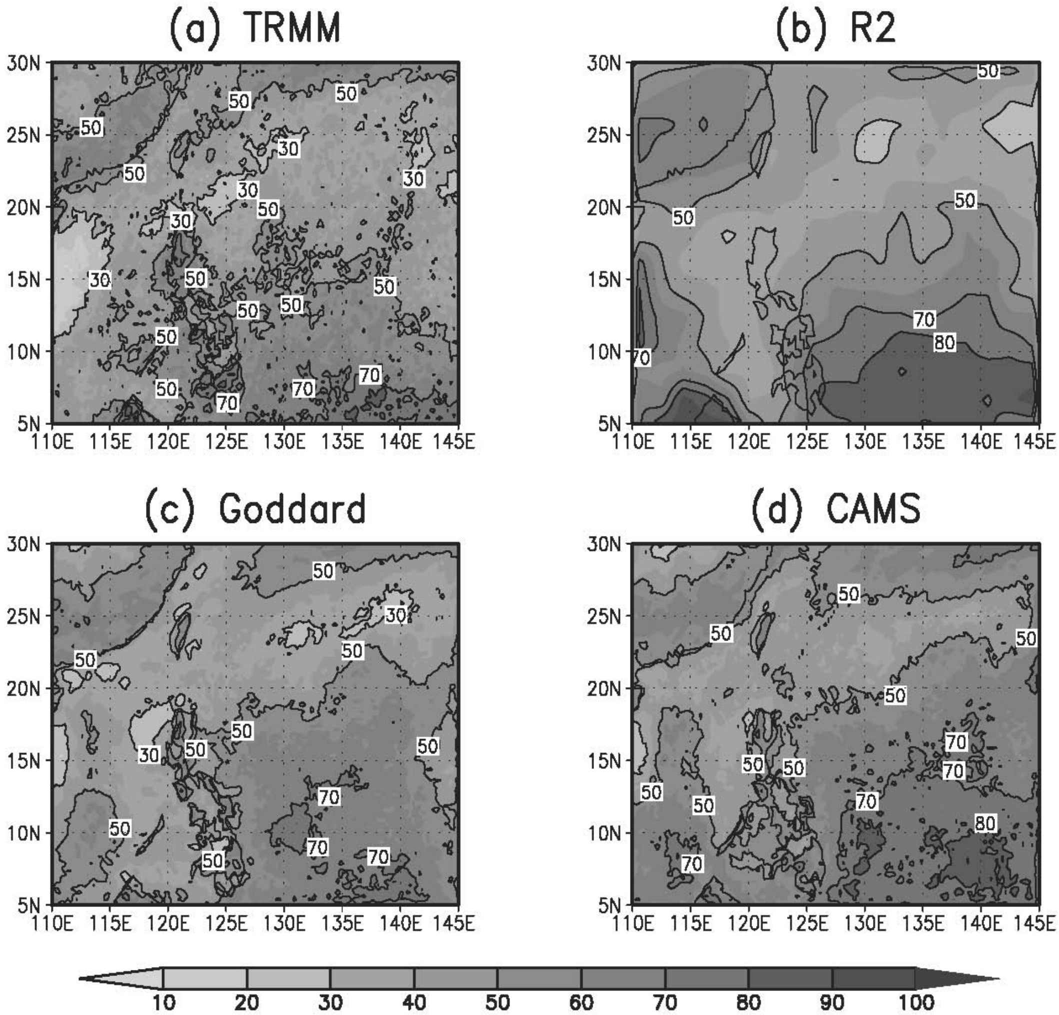

Figure 6. Percentage of days with precipitation rate exceeding 0.1 mm day^{-1} during May to June 2008 from (a) TRMM, (b) R2 reanalysis, and (c), (d) WRF simulations.

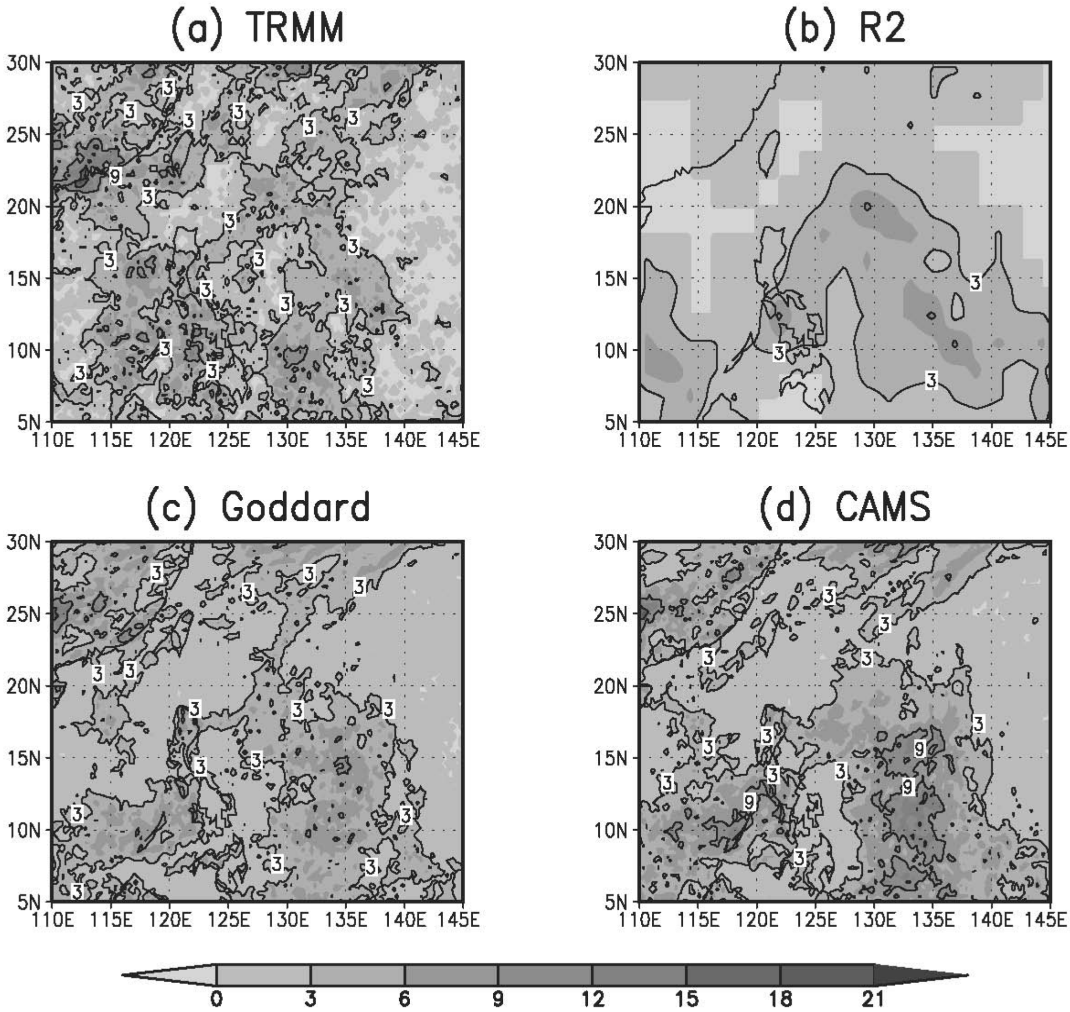

Figure 7. As Figure 6 but for precipitation rate exceeding 50 mm day^{-1}.

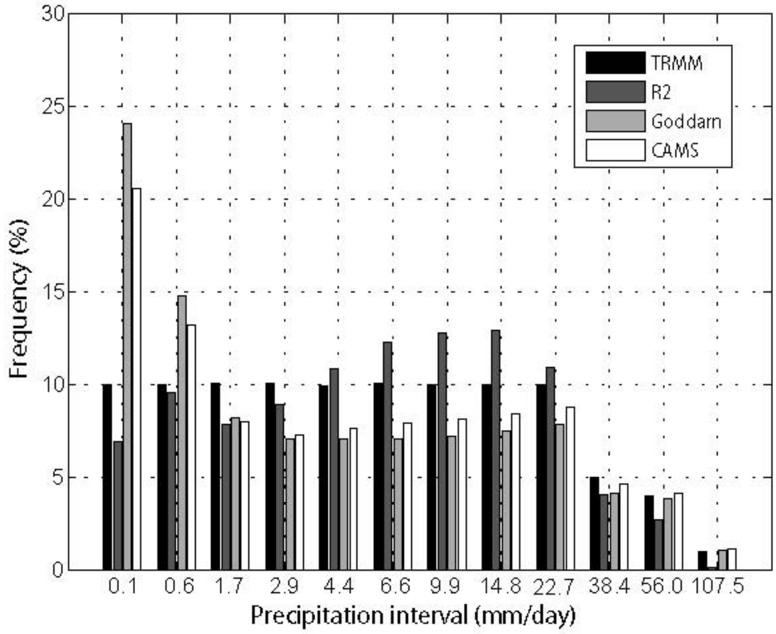

Figure 8. Probability distribution of observed and simulated daily precipitation at different intervals over domain 3.

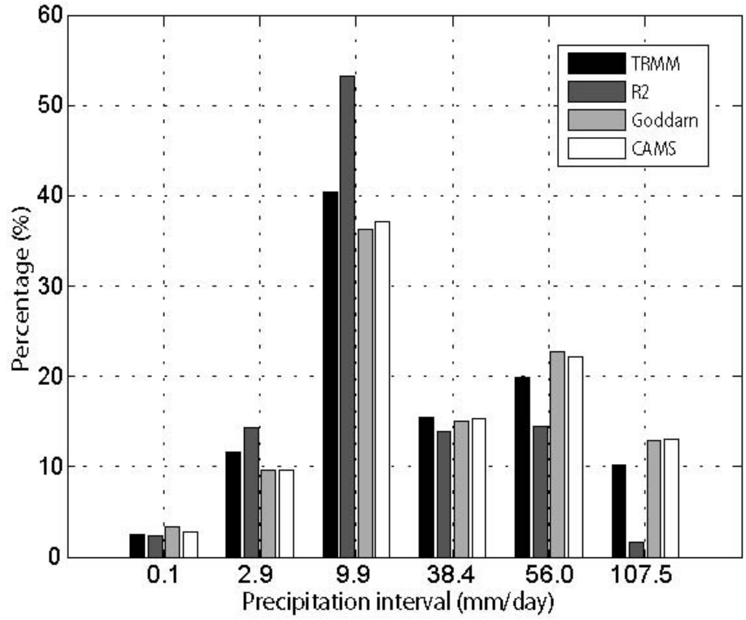

Figure 9. Percentage of observed and simulated precipitation amount as a function of precipitation rate over domain 3.

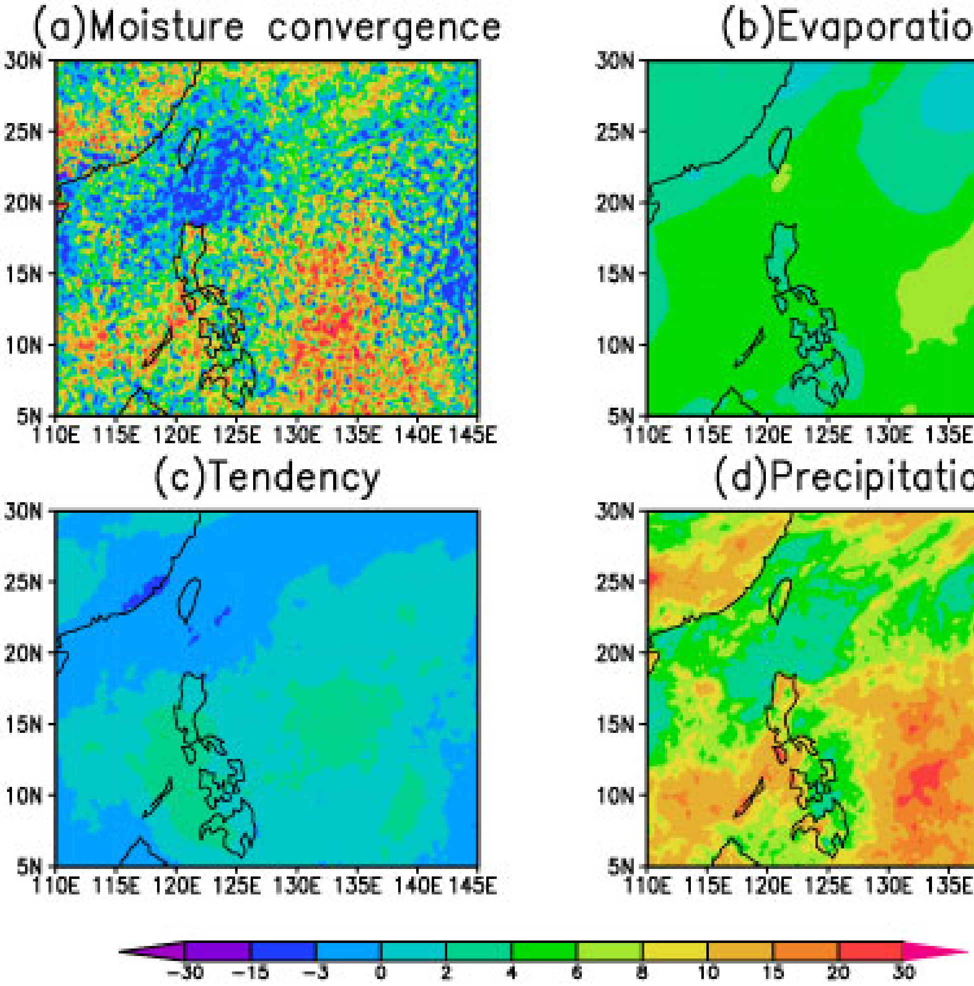

Figure 10. Daily mean (a) moisture convergence, (b) evaporation, (c) precipitable water tendency, and (d) precipitation (mm day^{-1}) derived from CAMS microphysics during May to June 2008.

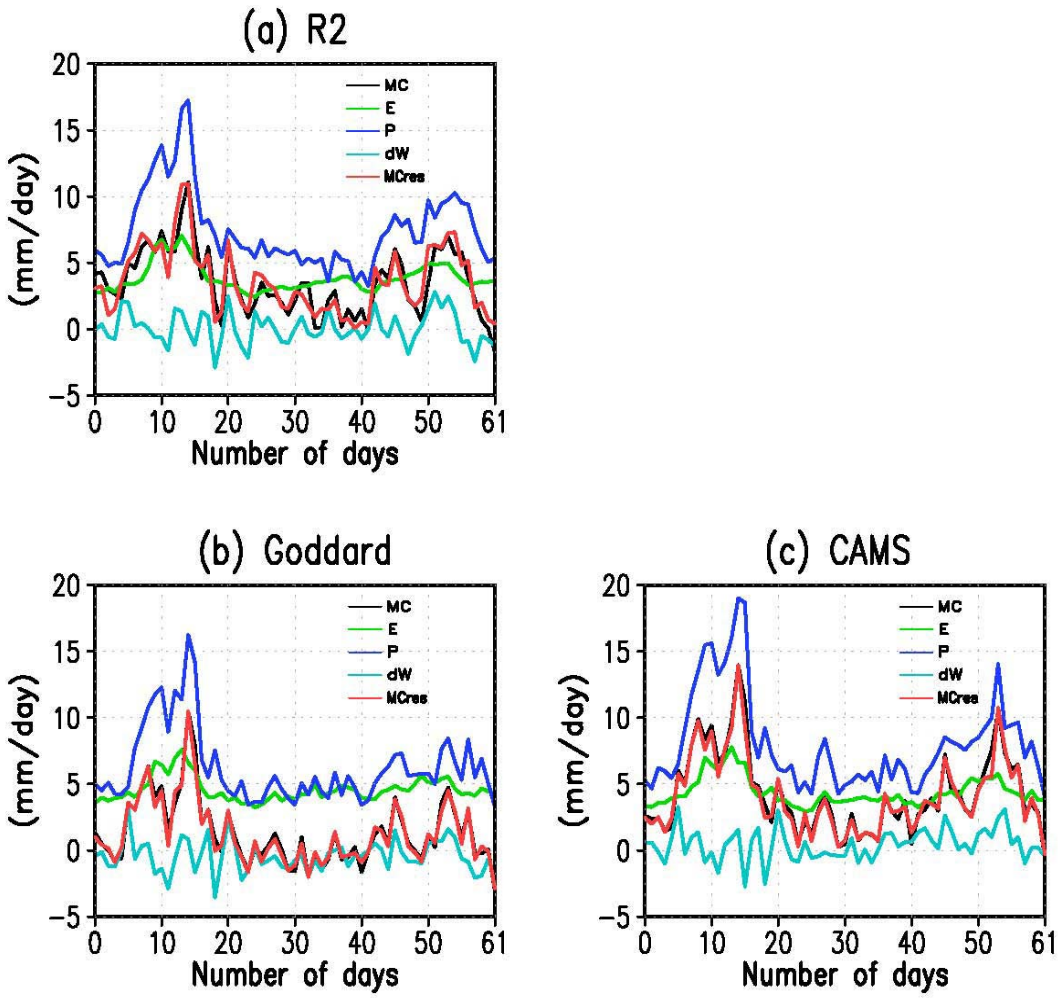

Figure 11. Time evolution of the daily mean moisture budget averaged over domain 3 from (a) R2 reanalysis, (b) Goddard, and (c) CAMS simulations.

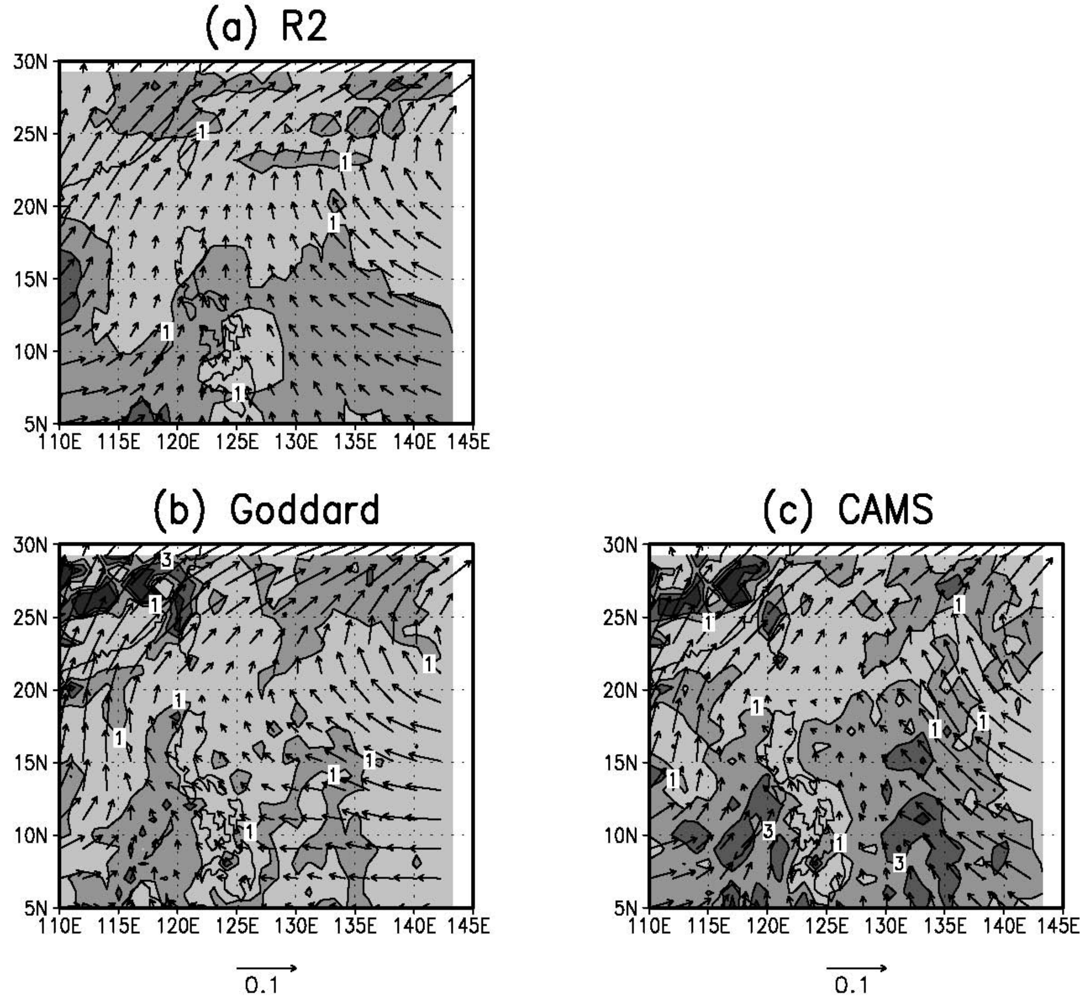

Figure 12. Mean 850 hPa moisture flux vector (m kg s^{-1} kg^{-1}) with associated moisture convergence fields (mm day^{-1}) averaged over May and June 2008 from (a) R2 reanalysis, (b) Goddard, and (c) CAMS simulations.

Table 1. Area-averaged daily mean precipitation (mm day^{-1}), pattern RMSE (mm day^{-1}) and pattern correlation coefficients between the observed and simulated daily mean precipitation shown in Figure 4.

	TRMM	R2	Goddard	CAMS
Mean	7.03	7.38	6.24	8.01
Spatial RMSE	-	4.20	3.26	4.00
Spatial correlation	-	0.26	0.53	0.48

Table 2. Area-averaged daily mean precipitation (mm day^{-1}), percentage of rainy days (%) and precipitation intensity (mm day^{-1}).

	TRMM	R2	Goddard	CAMS
Mean	7.03	7.38	6.24	8.01
Rainy days	47.4	55.6	49.1	57.1
Intensity	14.8	13.3	12.7	14.0

Table 3. The daily mean hydrologic budget terms averaged over domain 3 during May to June 2008.

	MC	E	P	dW
R2	3.03	3.86	7.38	0.05
Goddard	1.31	4.58	6.26	-0.45
CAMS	4.26	4.38	8.01	0.42